

A Monopole Mining Method for High Throughput Screening Weyl Semimetals

Vsevolod Ivanov and Sergey Y. Savrasov

Department of Physics, University of California, Davis, CA 95616, USA

(Dated: October 23, 2018)

Although topological invariants have been introduced to classify the appearance of protected electronic states at surfaces of insulators, there are no corresponding indexes for Weyl semimetals whose nodal points may appear randomly in the bulk Brillouin Zone (BZ). Here we use a well-known result that every Weyl point acts as a Dirac monopole and generates integer Berry flux to search for the monopoles on rectangular BZ grids that are commonly employed in self-consistent electronic structure calculations. The method resembles data mining technology of computer science and is demonstrated on locating the Weyl points in known Weyl semimetals. It is subsequently used in high throughput screening several hundreds of compounds and predicting a dozen new materials hosting nodal Weyl points and/or lines.

PACS numbers:

There has been recent surge of interest in topological quantum materials caused by the existence in these systems of robust electronic states insensitive to perturbations[1, 2]. Z_2 invariants have been proposed to detect the protected (quantum Hall-like) surface states in topological insulators (TIs) [3], and, for centrosymmetric crystals, this reduces to finding band parities of electronic wave functions at time-reversal invariant points in the Brillouin zone (BZ)[4]. For a general case, the calculation involves an integration of Berry fields [5], and has been implemented in numerical electronic structure calculations[6] with density functional theory. These methods have allowed for exhaustive searches to identify candidate materials hosting topological insulator phases [7–9].

Weyl semimetals (WSMs) are closely related systems characterized by a bulk band structure which is fully gapped except at isolated points described by the 2x2 Weyl Hamiltonian [2]. Sometimes these Weyl points extend into lines in the BZ giving rise to nodal line semimetals (NLSMs) [10]. Due to their intriguing properties such as Fermi arc surface states [11], chiral anomaly induced negative magnetoresistance [12], and a semi-quantized anomalous Hall effect [13, 14], the search for new WSM materials is currently very active. Unfortunately, their identification in infinite space of chemically allowed compounds represents a challenge: there is no corresponding topological index characterizing WSM phase, and the Weyl points may appear randomly in the bulk BZ. General principles, such as broken time reversal or inversion symmetry, or emergence of the WSM phase between topologically trivial and non-trivial insulating phases [11] are too vague to guide their high throughput screening, and recent group theoretical arguments[15, 16] to connect crystal symmetry with topological properties still await their practical realization. The progress in this field was mainly serendipitous, although the ideas based on band inversion mechanism[17] or analyzing mirror Chern numbers[18, 19] were proven to be useful in

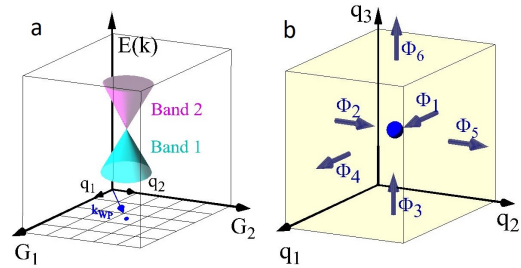


FIG. 1: a. A typical cone dispersion relationship $E(\mathbf{k})=\pm v|\mathbf{k}-\mathbf{k}_{\text{WP}}|$ for the Weyl point plotted within a rectangular area in \mathbf{k} -space set by divisions of reciprocal lattice translations \mathbf{G}_1 and \mathbf{G}_2 for a fixed value along the third translation \mathbf{G}_3 . b. The Weyl point located within a microcell set by the grid vectors $\mathbf{q}_1, \mathbf{q}_2, \mathbf{q}_3$ generates a Berry flux through each plaquette as given by the (right handed) circulation of the Berry connection with sign convention defined in text.

many recent discoveries[20–23], and computer oriented searches of topological semimetals are beginning to appear [24, 25].

In this work, we propose a straightforward method to identify Weyl semimetals by using a well-known result that every Weyl point acts as a Dirac monopole [26] producing a non-zero Berry flux when it is completely enclosed by a surface in the BZ. The enclosed charge is given by the chirality of the Weyl point similar to the Gauss theorem in the Coulomb law. Rectangular grids of \mathbf{k} -points that are widely employed in self-consistent electronic structure calculations for the BZ integration either via special points (Monkhorst-Pack) technique [27] or a tetrahedron method[28], are ideally suited for this purpose since they divide the volume of the BZ onto microcells and the electronic wave functions are automatically available at the corners of each microcell. It is thus a matter of rearranging the data to extract Berry phases of these wave functions in order to recover the Dirac monopoles inside the BZ. While there are some uncertainties connected to energy bands cutoffs used while

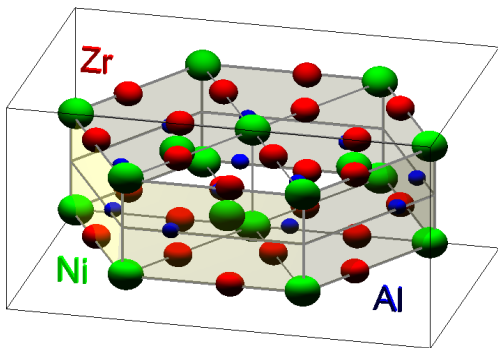


FIG. 2: ZrNiAl-type crystal structure (# 189 space group $p\bar{6}2m$) of noncentrosymmetric hexagonal compounds compounds studied in this work.

defining non-Abelian Berry fields for metallic systems, our method allows a subsequent refinement provided a signal from a monopole is detected. The entire procedure resembles data mining technology in computer science as an intelligent method to discover patterns from large data sets in a (semi-) automatic way so that the extracted data can subsequently be used in further analysis.

Since we are dealing with grids, there is a chance that the grid microcell will enclose both chiral positive and negative charges whose Berry fluxes cancel each other. Although resolution here is obviously adjustable by changing the grid size, and modern computers allow handlings of thousands and even millions of \mathbf{k} -points in parallel, going for Weyl points that are too close makes no sense from both practical and fundamental reasons. Practically, properties such as anomalous Hall effect[13, 14] are proportional to the distance between the Weyl points and so does the density of Fermi arc surface states[11]. Disorder, electronic interactions, thermal broadening and Heisenberg uncertainty principle provide fundamental limitations. Therefore, distances between the Weyl points need not be smaller than a few percent of the reciprocal lattice spacing, and this does not require dealing with very dense grids.

Here we implement this monopole mining method and test it by verifying locations of the Weyl points in several known systems, such as recently proposed TaAs[20] and CuF[23] Weyl semimetals. Next, we demonstrate how it can be used for high throughput screening of WSMs by scanning several hundreds of compounds in the $p\bar{6}2m$ (#189) space group with the ZrNiAl structure. We predict a dozen new materials hosting WSM/NLSM behavior.

We first outline the method to evaluate the Berry flux due to a single Weyl point that appears somewhere in the bulk BZ with its typical dispersion relationship $E(\mathbf{k}) = \pm v|\mathbf{k} - \mathbf{k}_{\text{WP}}|$ as illustrated in Fig.1a. We represent the BZ by reciprocal lattice translations $\mathbf{G}_{\nu=1,2,3}$

and divide it onto $N_1 \times N_2 \times N_3$ microcells. Each microcell is spanned by primitive vectors $\mathbf{q}_{\nu=1,2,3} = \mathbf{G}_{\nu}/N_{\nu}$ with its origin given by the grid of \mathbf{k} -points represented by three integers $n_{\nu} = 0, N_{\nu} - 1$ as $\mathbf{k} = n_1 \mathbf{q}_1 + n_2 \mathbf{q}_2 + n_3 \mathbf{q}_3$.

The problem of finding the wave vector \mathbf{k}_{WP} is reduced to recovering the microcell that contains the monopole. We define a non-Abelian link field that appears while evaluating the Berry phase using the finite difference method[6]

$$U_{\mathbf{q}}(\mathbf{k}) = \frac{\det [\langle \mathbf{k} + \mathbf{qj}' | e^{i\mathbf{q}\mathbf{r}} | \mathbf{kj} \rangle]}{|\det [\langle \mathbf{k} + \mathbf{qj}' | e^{i\mathbf{q}\mathbf{r}} | \mathbf{kj} \rangle]|} \quad (1)$$

Here the matrix elements between the periodic parts of the wave functions are cast into the form $\langle \mathbf{k} + \mathbf{qj}' | e^{i\mathbf{q}\mathbf{r}} | \mathbf{kj} \rangle$, which frequently appear in density functional linear response calculations[29] and thus are straightforward to evaluate. The set of energy bands j is spanned over occupied states and includes those that cross the Fermi level. However, some uncertainty exists in this enumeration procedure because the Berry flux from the negative and positive branches of the monopole (bands 1 and 2 for the example shown in Fig.1a) will cancel each other. For the example being discussed, this means that either band 1 or 2 (but not both) needs to be taken into account while evaluating Eq.1. In real materials, this may result in contribution for some monopoles cancelling, but since we are mostly interested in the Weyl points in the immediate vicinity of the Fermi level, varying the upper cutoff value for j by one or two will resolve this problem. We also note that the link field $U_{\mathbf{q}}(\mathbf{k})$ needs to be computed for the entire grid of \mathbf{k} -points, where the group symmetry operations help to generate the wave functions that are normally available within only irreducible portion of the BZ.

We now evaluate the Berry flux through faces of each microcell of the $N_1 \times N_2 \times N_3$ grid. This is illustrated in Fig.1b, where the flux $\Phi_{i=1..6}$ through each plaquette with the origin at particular \mathbf{k} and spanned by a pair of vectors $q_{\mu}q_{\nu}$ is conveniently encoded into the following formula

$$2\pi\Phi \equiv Im \ln \left[\frac{U_{\mathbf{q}_{\mu}}(\mathbf{k})U_{\mathbf{q}_{\nu}}(\mathbf{k} + \mathbf{q}_{\mu})}{U_{\mathbf{q}_{\nu}}(\mathbf{k})U_{\mathbf{q}_{\mu}}(\mathbf{k} + \mathbf{q}_{\nu})} \right] \quad (2)$$

This procedure is similar to one employed while evaluating Z_2 invariants [6] on six two-dimensional tori introduced in Ref. [30] but now the roles of the tori are played by the slices of the BZ spanned by each pair of the reciprocal vectors $G_{\mu}G_{\nu}$ with a fixed value along the third vector G_{ξ} . We only need to take care of the fact that the flux as given by Eq. 2 produces right (alternatively left) handed circulation of the Berry connection but inner (or outer) normal should be chosen consistently for the total flux through each surface of the microcell. Thus, the total Berry flux is given by

$$c = \Phi_1 + \Phi_2 + \Phi_3 - \Phi_4 - \Phi_5 - \Phi_6 \quad (3)$$

Although the flux through each plaquette is generally non-integer, the total flux is guaranteed to be an integer since individual contributions (2) from adjacent plaquettes cancel each other in Eq.(3), up to an addition of $2\pi n$. Therefore c returns either the chiral charge of the monopole or zero.

The entire algorithm is now viewed as an automated procedure that is either done following the self-consistent band structure calculation or "on the fly". We illustrate it on the example of TaAs Weyl semimetal whose electronic properties are well documented in recent literature [20]. We use a full potential linear muffin-tin orbital method (FP LMTO) developed by one of us [31] and perform a self-consistent density functional calculation with spin-orbit coupling using the Generalized Gradient Approximation [32]. We subsequently set up a k -grid using $20 \times 20 \times 20$ divisions of the reciprocal lattice unit cell. These types of grids were previously shown to be sufficient in calculating Z_2 invariants in topological insulators[33]. For evaluating the link field, Eq. (1), the energy window is chosen to span the entire valence band with the cutoff value corresponding to the band number that crosses the Fermi level. It appears this is sufficient to recover all monopoles. The net result is 24 out 8000 microcells produce non-zero Berry flux and give their approximate positions. We take the coordinates of the corresponding microcells (only non-equivalent by symmetry are needed; two for TaAs) and mine these areas of k -space by introducing similar rectangular grids inside each microcell in order to refine the locations of the Weyl points to the positions: (0.009, 0.506, 0), (0.019, 0.281, 0.579) in units $2\pi/a, 2\pi/a, 2\pi/c$. This is in agreement with the previous calculation [20].

We also considered CuF, recently predicted to be a Weyl semimetal by one of us[23]. The exact same setup ($20 \times 20 \times 20$ divisions with the energy panel spanned till the band that crosses the Fermi level) returns 24 microcells that are all related by symmetry. Zooming into one microcell returns the following location of the Weyl point: (0.281, 0.119, 0) $2\pi/a$, consistent with our previous result [23].

To demonstrate the predictive power of the method, we scanned several hundreds noncentrosymmetric hexagonal compounds in the $\bar{p}62m$ (# 189) space group with the ZrNiAl structure. A complete list of these materials is given in Supplementary Information. Topological electronic structures in few of these systems have already drawn a recent attention. CaAgP was predicted to be a line-node Dirac semimetal while CaAgAs was found to be a strong topological insulator [34]. Similar properties have been discussed for NaBaBi under pressure[35]. The unit cell of these crystals consists of a rhomboid prism with side a , internal angle $2\pi/3$, and height c ; the Ni-type atoms are located on the vertical edges and in the centers of the two equilateral triangles forming the rhombus base, with the Zr-type and Al-type atoms located on

TABLE I: List of non-equivalent Weyl and triple points (in units $2\pi/a, 2\pi/a, 2\pi/c$), their number and energies relative to the Fermi level (in eV) recovered using the monopole mining method for noncentrosymmetric hexagonal compounds in the $\bar{p}62m$ (# 189) space group with the ZrNiAl structure that are predicted to exhibit Weyl/nodal line semimetal behavior. The typical appearance of the Weyl points in the Brillouin Zone is cited by referencing to either sort A or B as illustrated in Fig. 3ab.

Comp.	Topological Points	Type	#	E (eV)
LaInMg	(0.00000, 0.36868, 0.01123)	Weyl-A	12	-0.06
LuGeAg	(0.00000, 0.42190, 0.00098)	Weyl-A	12	-0.23
YGeLi	(0.00000, 0.27793, 0.00817)	Weyl-A	12	-0.13
YPbAg	(0.00000, 0.40335, 0.03142)	Weyl-A	12	-0.09
YSiAg	(0.00000, 0.37864, 0.00384)	Weyl-A	12	-0.09
HfPRu	(0.46280, 0.06931, 0.0221)	Weyl-B	24	+0.06
ZrPRu	(0.45982, 0.07532, 0.01698)	Weyl-B	24	+0.06
LaTlMg	(0.00000, 0.38916, 0.03236)	Weyl-A	12	-0.13
	(0.41450, 0.02567, 0.00724)	Weyl-B	24	-0.13
YTlMg	(0.00000, 0.43303, 0.02319)	Weyl-A	12	-0.05
	(0.44076, 0.02908, 0.00441)	Weyl-B	24	-0.11
LuAsPd	(0.00000, 0.11481, 0.14140)	Weyl-A	12	+0.18
	(0.00000, 0.12004, 0.13942)	Weyl-A	12	+0.19
ZrAsOs	(0.47365, 0.02591, 0.04792)	Weyl-B	24	+0.02
	(0.47406, 0.01215, 0.04789)	Weyl-B	24	+0.02
TiGePd	(0.00000, 0.00000, 0.16495)	Triple	2	+0.14
	(0.00000, 0.00000, 0.20775)	Triple	2	+0.22
VAsFe	(0.00000, 0.000000, 0.32279)	Triple	2	+0.14
	(0.00000, 0.000000, 0.47625)	Triple	2	+0.19
	(0.00000, 0.38339, 0.17269)	Weyl-A	12	+0.09

the edges of these triangles, $1/3 \pm 1/4(c^2/a^2)$ away from the corners in the middle and bottom layers respectively [see Fig. 2]. We perform self-consistent band structure calculations and subsequent monopole mining procedure in exactly the same manner as we illustrated for TaAs and CuF. The lattice parameters can be found in Ref. [36].

Out of the compounds that we studied, we clearly identify 11 materials which show WSM behavior, 1 NLSM and 1 hosting both Weyl points and nodal lines. The two NLSMs also host topologically distinct triple fermion points [37]. Table I summarizes our results for each compound, giving the locations of the non-equivalent low-energy Weyl and/or triple points, their number and energies relative E_F in eV. The Weyl points are generally viewed as type II according to classification introduced in Ref. [38]. (Complete crystallographic and electronic structure data for these compounds is given in the supplementary information.)

Many of the Weyl semimetals that we predict in our work display remarkably similar locations of their Weyl points. LaInMg, LuGeAg, YGeLi, YPbAg, and YSiAg, exhibit 6 pairs (chiral positive and negative) of points, that are all symmetry related and are only slightly displaced from the $k_z = 0$ plane. They are located along the ΓM direction in the BZ. We illustrate their precise

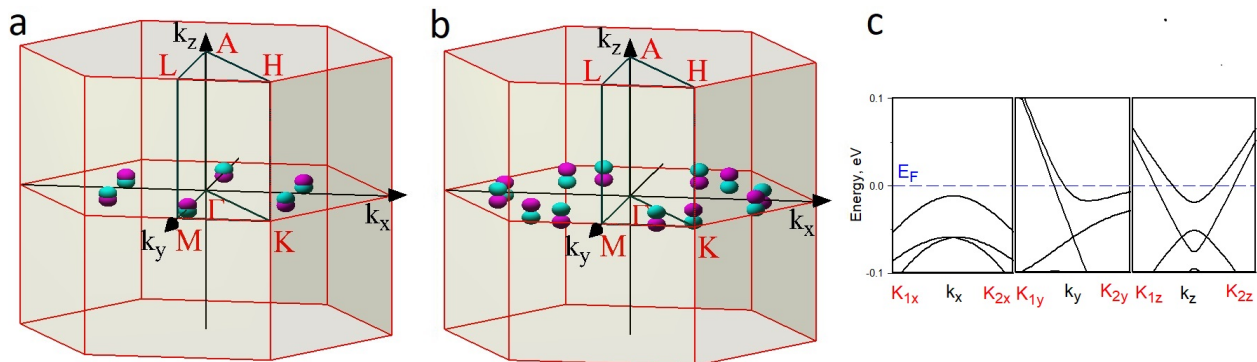


FIG. 3: a. Positions of 6 pairs (cyan for chiral positive and magenta for chiral negative) of low-energy Weyl points seen along the ΓM direction in the BZ for LaInMg and referenced in Table I as sort A; b. Positions of 12 pairs of Weyl points that are shifted symmetrically away from the ΓK line for HfPRu and referenced in Table I as sort B; c. Energy band dispersions in the vicinity of the Weyl point $k_{wpp} = (0.00000, 0.36868, 0.01123)$ for LaInMg. Point notations are as follows: $K_{1x} = (-0.10000, 0.36868, 0.01123)$, $K_{2x} = (0.10000, 0.36868, 0.01123)$, $K_{1y} = (0.0000, 0.26868, 0.01123)$, $K_{2y} = (0.0000, 0.46868, 0.011230)$, $K_{1z} = (0.0000, 0.36868, -0.056150)$, $K_{2z} = (0.0000, 0.36868, 0.056150)$ in units $2\pi/a, 2\pi/a, 2\pi/c$.

positions for LaInMg in Fig. 3a and refer to them in Table I as Weyl points of sort A. We find that HfPRu, and ZrPRu show another sort (referred to as sort B) of Weyl points, namely 12 pairs that are shifted symmetrically away from the ΓK line (see Fig. 3b). Interestingly, a similar behavior is seen for LaTiMg, and YTiMg which show both sorts (A and B) of Weyl points. LuAsPd shows two kinds of sort A Weyl points (24 total), while ZrAsOs shows two kinds of sort B Weyl points (48 total). Their displacement from $k_z = 0$ plane is much larger than the one found in previous cases. For each reported Weyl point, we also provide independent verification by calculating the band structures along k_x, k_y and k_z directions with the boundary vectors confining the Weyl point. An example of such plot is shown in Fig. 3c for the Weyl point in LaInMg, where one clearly recognizes the band crossings along all three directions that are characteristic of the Weyl cone dispersion.

Another interesting outcome of our high-throughput screening is the materials exhibiting nodal lines and triple-point fermions. TiGePd and VAsFe both host 12 pairs (chiral positive and negative) of nodal lines that are located very close to the ΓA direction in the BZ. We illustrate this behavior for TiGePd in Fig. 4a by zooming into the area of the BZ bounded by $0.15 \leq 2\pi k_z/c \leq 0.22$ and $-0.03 \leq 2\pi k_{x,y}/a \leq +0.03$. Interestingly, the nodal lines start and end at triple degenerate points that have recently enriched our classification of the topological objects [37]. These triple points are located at the ΓA line of the BZ. We provide their coordinates for TiGePd and VAsFe in Table I. The corresponding band structure plot for one of the triple points in TiGePd is shown in Fig. 4b along the k_x and k_y directions of the BZ with the boundary vectors confining the triple point. (A complete set of plots for each compound is provided in the supplementary information.)

tary information.)

One of the most striking features of Weyl semimetals is the presence of the Fermi arcs in their one-electron surface spectra[11]. Although computations of their shapes are possible via a self-consistent supercell (slab) calculation of the surface energy bands, given the number of compounds that we deal in this work, it is a computationally demanding study. Nevertheless, since the arcs connect the Weyl points of different chirality, one can expect that most of the materials that we list in Table I would have rather short arcs since the distances between positive and negative chiral charges are quite small. One notable exception is VAsFe which, as we list in Table I, exhibits not only nodal lines and triple points, but also a set of Weyl points which are well separated from each other. These are expected to produce very long Fermi arcs for the (100) or (110) crystallographic types of surfaces. One can also expect that their contribution to the anomalous Hall coefficient should be large since the latter is known to be directly proportional to the distance between the Weyl points [13]. We have recently shown [39] that long and straight Fermi arcs are generally capable of supporting nearly dissipationless surface currents, therefore it could be interesting to explore such possibility in VAsFe.

In conclusion, using the well-known property that Weyl points act as Dirac monopoles in k -space, we presented an automated monopole mining method to identify Weyl and nodal line semimetals. We tested the method by recovering the Weyl points in several known systems as well as demonstrating its predictive power by high throughput screening hundreds noncentrosymmetric hexagonal compounds in the $p62m$ (# 189) space group and finding 13 new materials whose electronic structures as well as the locations of the topological nodal points

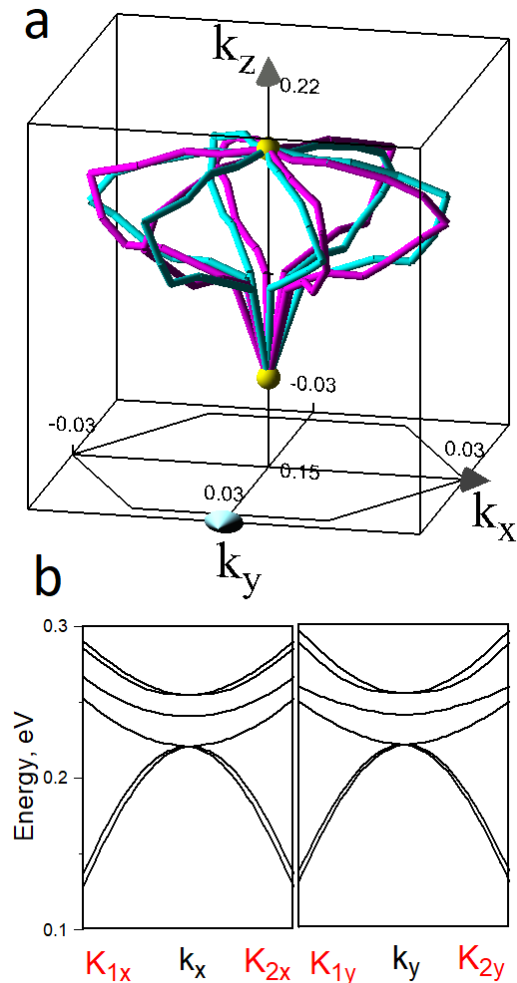


FIG. 4: a. A set of nodal lines for TiGePd that is recovered by the monopole mining method presented in this work. The color (cyan and magenta) distinguishes chiral positive and negative lines, respectively. The zoomed area of the BZ is bounded by $0.15 \leq 2\pi k_z/c \leq 0.22$ and $-0.03 \leq 2\pi k_{x,y}/a \leq +0.03$. Also shown in yellow are the triple degenerate topological points [37]. b. Energy band dispersions in the vicinity of the triple point $(0, 0, 0.20775)$ for TiGePd. Point notations are as follows: $K_{1x} = (-0.10000, 0.0000, 0.20775)$, $K_{2x} = (0.10000, 0.0000, 0.20775)$, $K_{1y} = (0.0000, -0.10000, 0.20775)$ in units $2\pi/a, 2\pi/a, 2\pi/c$.

and lines have been reported. As we judge from our calculated energy bands, the WSMs identified in this work exhibit regular Fermi surface states while the Weyl points are not exactly pinned at the Fermi level. This is similar to other recently discovered WSMs, such as TaAs[20] whose experimental studies of large negative magnetoresistance have been recently performed[40]. Despite the latter representing a signature of the much celebrated chiral anomaly feature in Weyl semimetals, there exists an obvious problem of distinguishing contributions from the Weyl points and regular Fermi states. In this regard our automated approach should be helpful for scanning

vast material databases in identifying an ideal WSM with only nodal points at the Fermi level as it was originally envisioned in pyrochlore iridates[11].

The work was supported by NSF DMR Grant No. 1411336.

-
- [1] For a review, see, e.g., M. Z. Hasan, C. L. Kane, Colloquium: Topological insulators, *Rev. Mod. Phys.* **82**, 3045 (2010).
 - [2] For a review, see, e.g., N.P. Armitage, E. J. Mele, A. Vishwanath, Weyl and Dirac Semimetals in Three Dimensional Solids, *Rev. Mod. Phys.* **90**, 15001 (2018).
 - [3] C. L. Kane and E. J. Mele, Z_2 Topological Order and the Quantum Spin Hall Effect, *Phys. Rev. Lett.* **95**, 226801 (2005).
 - [4] L. Fu and C. L. Kane, Topological insulators with inversion symmetry, *Phys. Rev. B* **76**, 045302 (2007).
 - [5] L. Fu and C. L. Kane, Time reversal polarization and a Z_2 adiabatic spin pump, *Phys. Rev. B* **74**, 195312 (2006).
 - [6] T. Fukui and Y. Hatsugai, Quantum Spin Hall Effect in Three Dimensional Materials: Lattice Computation of Z_2 Topological Invariants and Its Application to Bi and Sb, *Journal Phys. Soc. Japan* **76**, 053702 (2007).
 - [7] H. Lin, L. A. Wray, Y. Xia, S. Xu, S. Jia, R. J. Cava, A. Bansil, and M. Z. Hasan, Half-Heusler ternary compounds as new multifunctional experimental platforms for topological quantum phenomena, *Nature Materials* **9**, 546 (2010).
 - [8] S. Chadov, X. Qi, J. Kubler, G. H. Fecher, C. Felser, and S. C. Zhang, Tunable multifunctional topological insulators in ternary Heusler compounds, *Nature Materials* **9**, 541 (2010).
 - [9] M. G. Vergniory, L. Elcoro, C. Felser, B. A. Bernevig, Z. Wang, The (High Quality) Topological Materials In The World, arXiv:1807.10271.
 - [10] A. A. Burkov, M.D. Hook, and L. Balents, Topological nodal semimetals, *Phys. Rev. B* **84**, 235126 (2011).
 - [11] X. Wan, A. M. Turner, A. Vishwanath, and S. Y. Savrasov, Topological semimetal and Fermi-arc surface states in the electronic structure of pyrochlore iridates, *Phys. Rev. B* **83**, 205101 (2011).
 - [12] H. B. Nielsen and M. Ninomiya, The Adler-Bell-Jackiw anomaly and Weyl fermions in a crystal, *Phys. Lett.* **130 B**, 389 (1983).
 - [13] Kai-Yu Yang, Yuan-Ming Lu, and Ying Ran, Quantum Hall effects in a Weyl semimetal: Possible application in pyrochlore iridates, *Phys. Rev. B* **84**, 075129 (2011).
 - [14] A. A. Burkov, L. Balents, Weyl Semimetal in a Topological Insulator Multilayer, *Phys. Rev. Lett.* **107**, 127205 (2011).
 - [15] H. C. Po, A. Vishwanath, H. Watanabe, Symmetry based Indicators of Band Topology in the 230 Space Groups, *Nat. Commun.* **8**, 50 (2017).
 - [16] J. Krutho, J. de Boer, J. van Wezel, C. L. Kane, and R.-J. Slager, Topological Classification of Crystalline Insulators through Band Structure Combinatorics, *Phys. Rev. X* **7**, 041069 (2017).
 - [17] B. A. Bernevig, T. L. Hughes, S.-C. Zhang, Quantum Spin Hall Effect and Topological Phase Transition in HgTe Quantum Wells, *Science* **314**, 1757 (2006).

- [18] T. H. Hsieh, H. Lin, J. Liu, W. Duan, A. Bansil, and L. Fu, Topological Crystalline Insulators in the SnTe Material Class, *Nat. Commun.* **3**, 982 (2012).
- [19] H. Weng, J. Zhao, Z. Wang, Z. Fang, and X. Dai, Topological Crystalline Kondo Insulator in Mixed Valence Ytterbium Borides, *Phys. Rev. Lett.* **112**, 016403 (2014).
- [20] B. Q. Lv, H. M. Weng, B. B. Fu, X.P. Wang, H. Miao, J. Ma, P. Richard, X. C. Huang, L. X. Zhao, G. F. Chen, Z. Fang, X. Dai, T. Qian, and H. Ding, Experimental discovery of Weyl semimetal TaAs, *Phys. Rev. X* **5**, 031013 (2015).
- [21] Lunan Huang, Timothy M. McCormick, Masayuki Ochi, Zhiying Zhao, Michi-To Suzuki, Ryotaro Arita, Yun Wu, Daixiang Mou, HuiBo Cao, Jiaqiang Yan, Nandini Trivedi, Adam Kaminski, Spectroscopic evidence for a type II Weyl semimetallic state in MoTe₂, *Nature Materials* **15**, 1155 (2016).
- [22] Guoqing Chang, Su-Yang Xu³, Daniel S. Sanchez, Shin-Ming Huang, Chi-Cheng Lee, Tay-Rong Chang, Guang Bian, Hao Zheng, Ilya Belopolski, Nasser Alidoust, Horng-Tay Jeng, Arun Bansil, Hsin Lin, M. Zahid Hasan, A strongly robust type II Weyl fermion semimetal state in Ta₃S₂, *Science Advances* **2**, e1600295 (2016).
- [23] Y. Du, E.-J. Kan, H. Xu, S. Y. Savrasov, X. Wan, Turning Copper Metal into Weyl Semimetal, *Phys. Rev. B* **97**, 245104 (2018).
- [24] D. Gresch, G. Autes, O. V. Yazyev, M. Troyer, D. Vanderbilt,, B. A. Bernevig, and A. A. Soluyanov, Z2Pack: Numerical implementation of hybridWannier centers for identifying topological materials, *Phys. Rev. B* **95**, 075146 (2017).
- [25] Zhang T, Jiang Y, Song Z, Huang H, He Y, et al. Catalogue of topological electronic materials, arXiv:1807.08756.
- [26] Z. Fang, N. Nagaosa, K. S. Takahashi, A. Asamitsu, R. Mathieu, T. Ogasawara, H. Yamada, M. Kawasaki, Y. Tokura, K. Terakura, The Anomalous Hall Effect and Magnetic Monopoles in Momentum Space, *Science* **302**, 92 (2003).
- [27] H. J. Monkhorst and J. D. Pack, Special points for Brillouin-zone integrations, *Phys. Rev. B* **13**, 5188 (1976).
- [28] O. Jepsen and O. K. Andersen, No error in the tetrahedron integration scheme, *Phys. Rev. B* **29**, 5965 (1984).
- [29] S. Y. Savrasov, Linear-response calculations of lattice dynamics using muffin-tin basis sets, *Phys. Rev. Lett.* **69**, 2819 (1992).
- [30] J. E. Moore and L. Balents, Topological invariants of time-reversal-invariant band structures, *Phys. Rev. B* **75**, 121306 (2007).
- [31] S. Y. Savrasov, Linear-response theory and lattice dynamics: a muffin-tin-orbital approach, *Phys. Rev. B* **54**, 16470 (1996).
- [32] J. P. Perdew, K. Burke, M. Ernzerhof, Generalized Gradient Approximation Made Simple, *Phys. Rev. Lett.* **77**, 3865 (1996).
- [33] W. Fenga, J. Wend, J. Zhoua, D. Xiao, Y. Yao, First-principles calculation of Z₂ topological invariants within the FP-LAPW formalism, *Comp. Phys. Comm.* **183** 1849 (2012).
- [34] A. Yamakage, Y. Yamakawa, Y. Tanaka, and Y. Okamoto, Line-Node Dirac Semimetal and Topological Insulating Phase in Noncentrosymmetric Pnictides CaAgX (X = P, As), *J. Phys. Soc. Jpn.* **85**, 013708 (2016).
- [35] Y. Sun, Q.-Z. Wang, S.-C. Wu, C. Felser, C.-X. Liu, B. Yan, Pressure-induced topological insulator in NaBaBi with right-handed surface spin texture, *Phys. Rev. B* **93**, 205303 (2016).
- [36] Handbook of Inorganic Substances, edited by Pierre Villars, Karin Cenzual & Roman Gladyshevskii (De Gruyter, 2015).
- [37] Z. Zhu, G. W. Winkler, Q.-S. Wu, J. Li, A. A. Soluyanov, Triple Point Topological Metals, *Phys. Rev. X* **6**, 031003 (2016).
- [38] A. A. Soluyanov, D. Gresch, Z. Wang, Q. Wu, M. Troyer, X. Dai and B. A. Bernevig, Type-II Weyl semimetals, *Nature* **527**, 495 (2015).
- [39] G. Resta, S.-T. Pi, X. Wan, and S. Y. Savrasov, High surface conductivity of Fermi-arc electrons in Weyl semimetals, *Phys. Rev. B* **97**, 085142 (2018).
- [40] X. Huang, L. Zhao, Y. Long, P. Wang, D. Chen, Z. Yang, H. Liang, M. Xue, H. Weng, Z. Fang, X. Dai, and G. Chen, Observation of the Chiral-Anomaly-Induced Negative Magnetoresistance in 3D Weyl Semimetal TaAs, *Phys. Rev. X* **5**, 031023 (2015).

SUPPLEMENTARY INFORMATION

List of Compounds

Here we list noncentrosymmetric hexagonal compounds in the $p\bar{6}2m$ (# 189) space group with the ZrNiAl structure studied in this work. Their complete crystallographic data can be found in Ref. [1]. As many of the compounds in this structure include rare earth elements with their f electron states appearing in the vicinity of the Fermi level, we first provide a list of only those compounds that do not explicitly include Lanthanides (see Table I). These are the systems for which density functional based calculations can be trusted in general.

We can also comment on the compounds that include Lanthanide elements. They can be separated onto two large groups. The first group includes the materials where the narrow f-band appears crossing the Fermi level in the calculated band structures. This would be an indication that a many-body renormalization of the single particle spectra (such, e.g., as band narrowing, multiplet transitions, etc) is expected. Although modern electronic structure approaches based on combinations of density functional and dynamical mean field theories [2] allow handling such cases, those are outside the scope of the present study, and we do not study topological properties of these compounds. The second group includes the materials with either fully empty or fully occupied f band, namely f^0 : LaAuCd, LaAuIn, LaAuMg, LaCuIn, LaCuMg, LaInMg, LaIrSn, LaNiIn, LaNiZn, LaPdCd, LaPdHg, LaPdIn, LaPdMg, LaPdPb, LaPdSn, LaPdTl, LaPtIn, LaPtPb, LaPtSn, LaRhIn, LaRhSn, LaTiMg; f^{14} : LuAsPd, LuAuIn, LuAuZn, LuCuIn, LuGaMg, LuGeAg, LuGeLi, LuInMg, LuIrSn, LuNiAl, LuNiIn, LuNiPb, LuPbAg, LuPdIn, LuPdSn, LuPdZn, LuPtIn, LuPtSn, LuRhSn, LuSiAg, LuTiMg. These are the cases where static mean field description can in principle capture single particle excitations (apart from the question whether the position of the f-band is correctly predicted by such theory).

There are a few materials that include Sm ion with its non-magnetic configuration f^6 : SmAgMg, SmAuCd, SmAuIn, SmAuMg, SmCuAl, SmCuIn, SmIrIn, SmIrSn, SmNiAl, SmNiIn, SmNiSn, SmNiZn, SmPdCd, Sm-

PdHg, SmPdIn, SmPdMg, SmPdPb, SmPdTl, SmPtIn, SmPtMg, SmPtPb, SmPtSn, SmRhIn, SmRhSn, SmSiAg, SmTiMg. Here $j = 5/2$ and $j = 7/2$ subbands appear below and above the Fermi level, respectively. The Coulomb renormalization in these compounds has a predictable effect by renormalizing the spin-orbit coupling by the Hubbard-type interaction, and the states in the immediate vicinity of the Fermi level are not affected.

TABLE I: List of noncentrosymmetric hexagonal compounds in the $p\bar{6}2m$ (# 189) space group with the ZrNiAl structure studied in this work. The compounds containing Lanthanide element are explicitly excluded from the Table.

Class	X =	Class	X =
CrAsX	Ti, Pd, Fe, Co, Ni, Rh	XPtIn	Sc, Y
MnAsX	Ti, Ni, Rh, Fe, Pd, Ru	TiGeX	Co, Pd
ScGeX	Fe, Rh, Cu, Os, Pd, Ru	ZrCoX	Ga, Sn
XSiRe	Hf, Ta, Ti, Zr	ZrGeX	Os, Zn
HfGeX	Fe, Os, Rh, Ru	XNiGa	Hf, Zr
FeAsX	Ti, Co, V, Ni	ScPX	Ir, Na
XPNi	Fe, Mo, W, Co	MnGeX	Pd, Rh
XGeMn	Hf, Nb, Sc, Ta	CrPX	Pd, Ni
TiPX	Cr, Os, Ru	HfXRu	P, As
ZrPX	Os, Mo, Ru	XAsOs	Hf, Zr
MnPX	Rh, Pd, Ni	XPdPb	Ca, Y
ScSiX	Cu, Ru, Mn	XSiMn	Nb, Ta
CaXCd	Ge, Sn, Pb	HfSiX	Os, Ru
XAsPd	Hf, Ti, Zr	CaXAg	P, As
XNiAl	Hf, Y, Zr	ZrXRu	Si, As
XBFe	Nb, Ta	NbCrX	Ge, Si
Other: YRhSn, YAuCd, YPdMg, YNiIn, ScGeAg			
YPdAl, YInMg, YAuZn, YPbAg, YPdTi			
YAuMg, YPdZn, YPdTl, YSiAg, YRhIn			
YTiMg, YAgMg, YAuIn, YCuIn, YGaMg			
HfIrSn, YPdIn, YCuAl, YGeLi, YPtSn			
YCuMg, BaBiNa, YAlMg, ScSnAg, YSiLi			

Data for Topological Points

Figures 1–13 provide complete data for the topological materials predicted in this work: the band structures near the Fermi level, energy panels used for defining non-Abelian Berry connection, positions of low-energy topological nodal points in the Brillouin Zone as well as energy band dispersions in the vicinity of the nodal points.

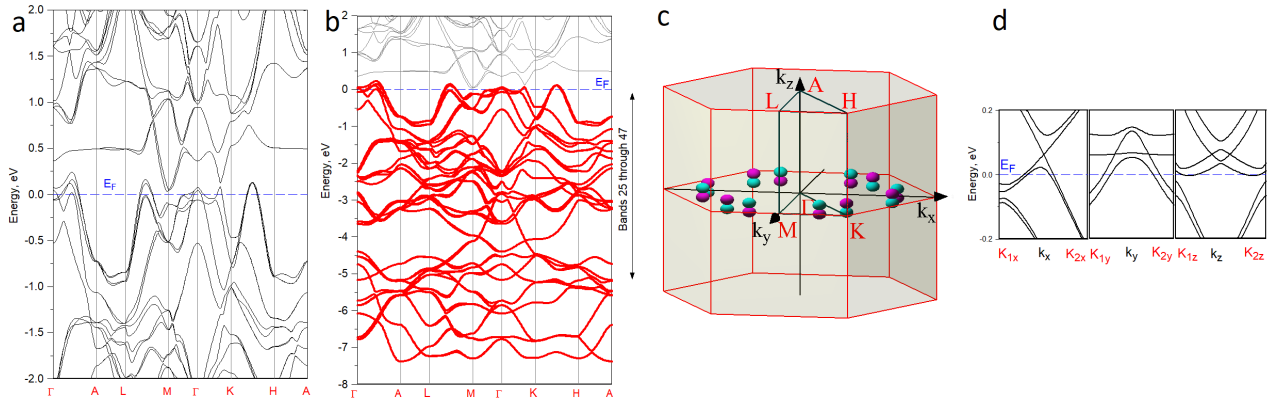


FIG. 1: Results for HfPRu: a. band structure near the Fermi level; b. energy panel used for defining non-Abelian Berry connection; c. positions of low-energy Weyl points as well as d. energy band dispersions in the vicinity of the Weyl point $k_{wp} = (0.46280, 0.06931, 0.02210)$. Point notations are as follows: $K_{1x} = (0.36280, 0.069310, 0.022100)$, $K_{2x} = (0.56280, 0.069310, 0.022100)$, $K_{1y} = (0.46280, -0.17328, 0.02210)$, $K_{2y} = (0.46280, 0.17328, 0.022100)$, $K_{1z} = (0.46280, 0.06931, -0.11050)$, $K_{2z} = (0.46280, 0.06931, 0.11050)$ in units $2\pi/a, 2\pi/a, 2\pi/c$. Lattice parameters used: $a=12.1207$ a.u., $c/a=0.58513$ [3].

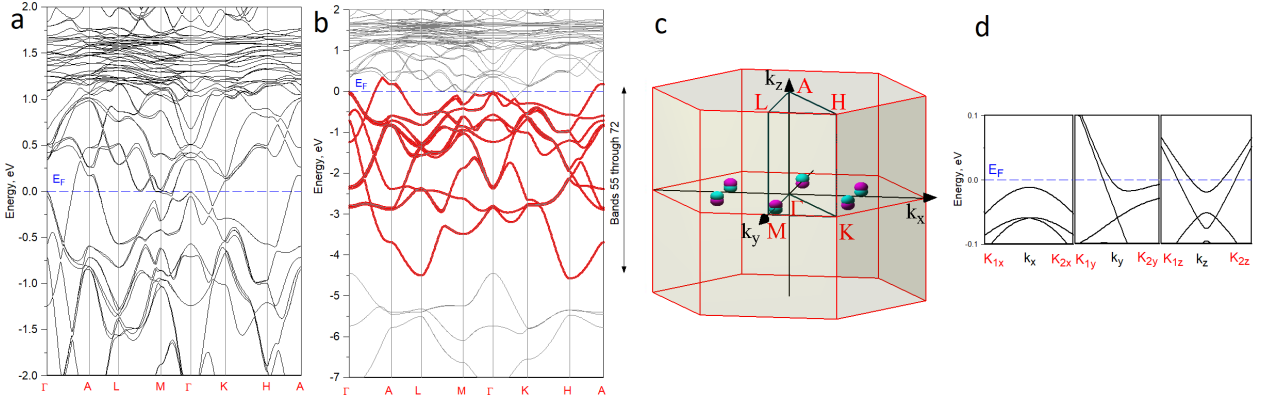


FIG. 2: Results for LaInMg: a. band structure near the Fermi level; b. energy panel used for defining non-Abelian Berry connection; c. positions of low-energy Weyl points as well as d. energy band dispersions in the vicinity of the Weyl point $k_{wp} = (0.00000, 0.36868, 0.01123)$. Point notations are as follows: $K_{1x} = (-0.10000, 0.36868, 0.01123)$, $K_{2x} = (0.10000, 0.36868, 0.01123)$, $K_{1y} = (0.0000, 0.26868, 0.01123)$, $K_{2y} = (0.0000, 0.46868, 0.011230)$, $K_{1z} = (0.0000, 0.36868, -0.056150)$, $K_{2z} = (0.0000, 0.36868, 0.056150)$ in units $2\pi/a, 2\pi/a, 2\pi/c$. Lattice parameters used: $a=14.789$ a.u., $c/a=0.61472$ [4].

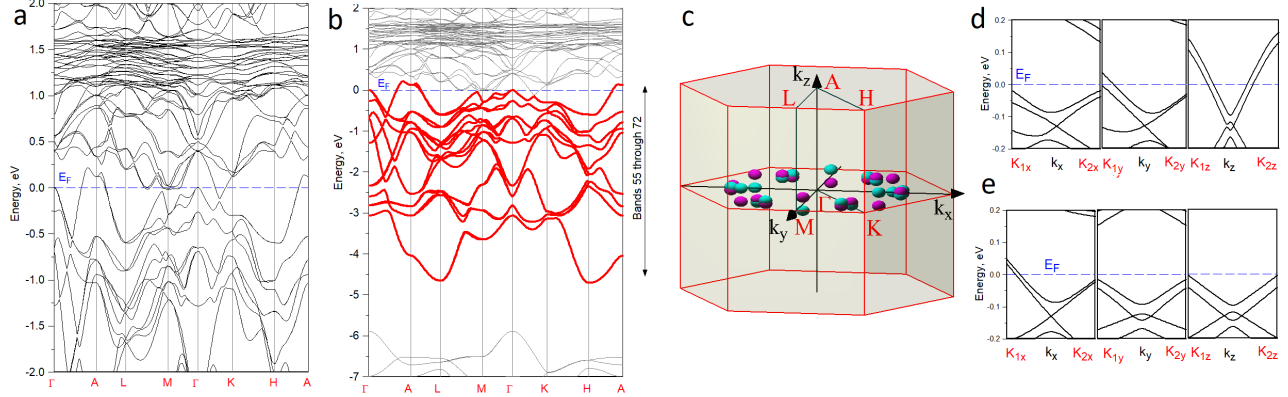


FIG. 3: Results for LaTiMg: a. band structure near the Fermi level; b. energy panel used for defining non-Abelian Berry connection; c. positions of low-energy Weyl points; d. energy band dispersions in the vicinity of the Weyl point $k_{wp} = (0.0000, 0.38916, 0.03236)$. Points notations are as follows: $K_{1x} = (-0.10000, 0.38916, 0.032360)$, $K_{2x} = (0.10000, 0.38916, 0.032360)$, $K_{1y} = (0.0000, 0.28916, 0.03236)$, $K_{2y} = (0.0000, 0.48916, 0.03236)$, $K_{1z} = (0.0000, 0.38916, -0.16180)$, $K_{2z} = (0.0000, 0.38916, 0.16180)$ in units $2\pi/a, 2\pi/a, 2\pi/c$ as well as e. energy band dispersions in the vicinity of the Weyl point $k_{wp} = (0.41450, 0.02567, 0.00724)$. Point notations are as follows: $K_{1x} = (0.3145, 0, 0.02567, 0.00724)$, $K_{2x} = (0.51450, 0.02567, 0.00724)$, $K_{1y} = (0.41450, -0.12835, 0.00724)$, $K_{2y} = (0.41450, 0.12835, 0.00724)$, $K_{1z} = (0.41450, 0.02567, -0.0362)$, $K_{2z} = (0.41450, 0.02567, 0.0362)$ in units $2\pi/a, 2\pi/a, 2\pi/c$. Lattice parameters used: $a=14.7644$ a.u., $c/a=0.61160$ [5].

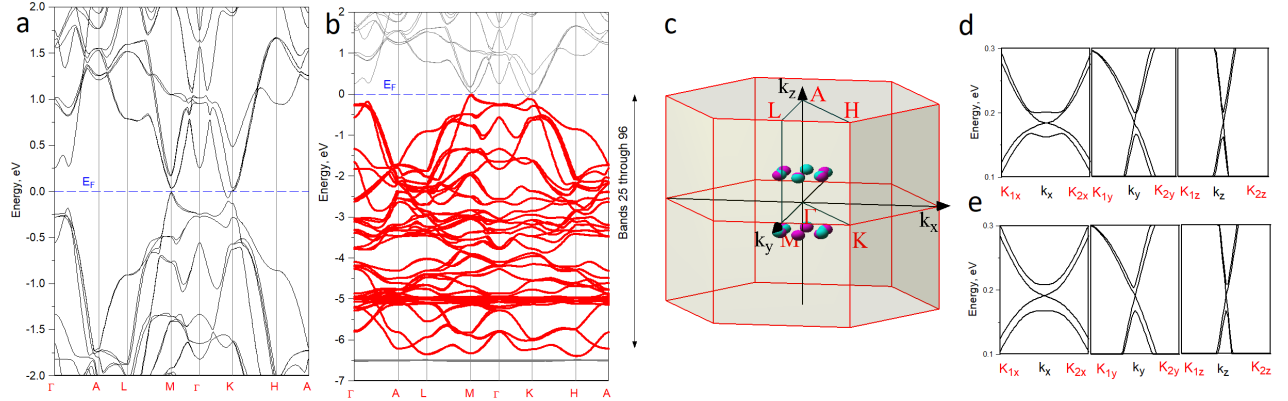


FIG. 4: Results for LuAsPd: a. band structure near the Fermi level; b. energy panel used for defining non-Abelian Berry connection; c. positions of low-energy Weyl points as well as d. energy band dispersions in the vicinity of the Weyl point $k_{wp} = (0.00000, 0.11481, 0.14140)$. Points notations are as follows: $K_{1x} = (-0.10000, 0.11481, 0.14140)$, $K_{2x} = (0.10000, 0.11481, 0.14140)$, $K_{1y} = (0.0000, 0.01481, 0.14140)$, $K_{2y} = (0.0000, 0.21481, 0.14140)$, $K_{1z} = (0.0000, 0.11481, 0.0414)$, $K_{2z} = (0.0000, 0.11481, 0.24140)$ in units $2\pi/a, 2\pi/a, 2\pi/c$. Lattice parameters used: $a=13.1733$ a.u., $c/a=0.55817$ [6].

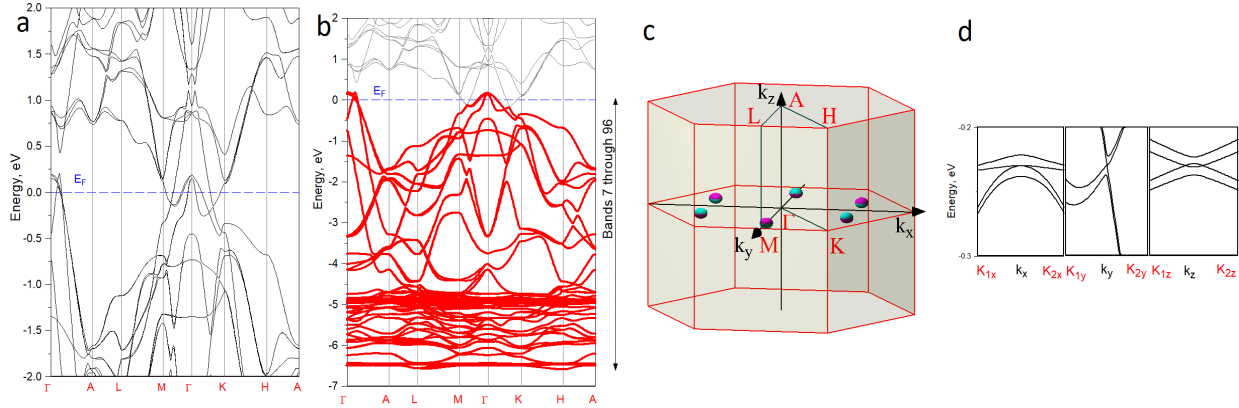


FIG. 5: Results for LuGeAg: a. band structure near the Fermi level; b. energy panel used for defining non-Abelian Berry connection; c. positions of low-energy Weyl points as well as d. energy band dispersions in the vicinity of the Weyl point $k_{wp} = (0.00000, 0.42190, 0.00098)$. Point notations are as follows: $K_{1x} = (-0.10000, 0.42190, 0.00098)$, $K_{2x} = (0.10000, 0.42190, 0.00098)$, $K_{1y} = (0.0000, 0.32190, 0.00098)$, $K_{2y} = (0.0000, 0.52190, 0.00098)$, $K_{1z} = (0.0000, 0.42190, -0.0049)$, $K_{2z} = (0.0000, 0.42190, 0.0049)$ in units $2\pi/a, 2\pi/a, 2\pi/c$. Lattice parameters used: $a=13.2517$ a.u., $c/a=0.58948$ [7].

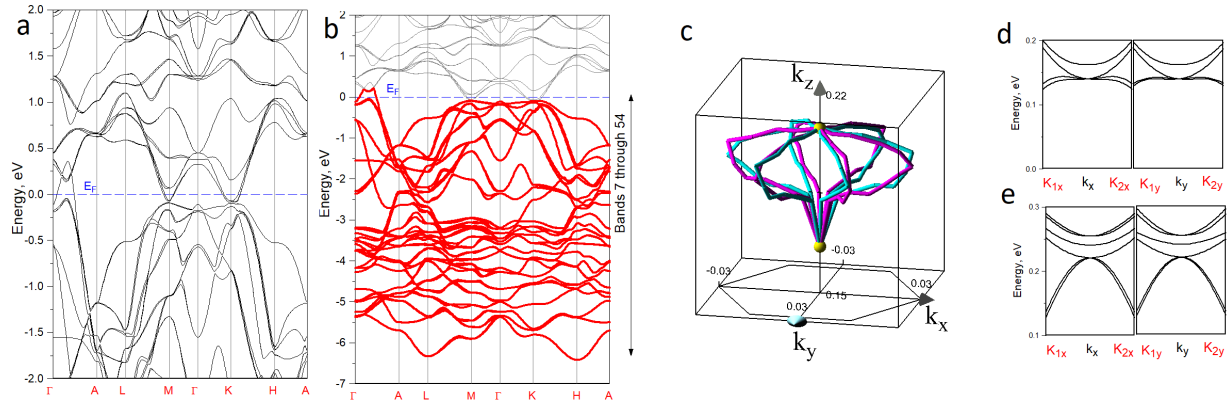


FIG. 6: Results for TiGePd: a. band structure near the Fermi level; b. energy panel used for defining non-Abelian Berry connection; c. nodal lines and positions of triple degenerate points. The zoomed area of the BZ is bounded by $0.15 \leq 2\pi k_z/c \leq 0.22$ and $-0.03 \leq 2\pi k_{x,y}/a \leq +0.03$; d. energy band dispersions in the vicinity of the triple point $k_{tp} = (0.00000, 0.00000, 0.16495)$. Points notations are as follows: $K_{1x} = (-0.10000, 0.0000, 0.16495)$, $K_{2x} = (0.10000, 0.0000, 0.16495)$, $K_{1y} = (0.0000, -0.10000, 0.16495)$, $K_{2y} = (0.0000, 0.10000, 0.16495)$ in units $2\pi/a, 2\pi/a, 2\pi/c$; e. energy band dispersions in the vicinity of the triple point $k_{tp} = (0.00000, 0.00000, 0.20775)$. Point notations are as follows: $K_{1x} = (-0.10000, 0.0000, 0.20775)$, $K_{2x} = (0.10000, 0.0000, 0.20775)$, $K_{1y} = (0.0000, -0.10000, 0.20775)$ in units $2\pi/a, 2\pi/a, 2\pi/c$. Lattice parameters used: $a=12.4779$ a.u., $c/a=0.56032$ [8].

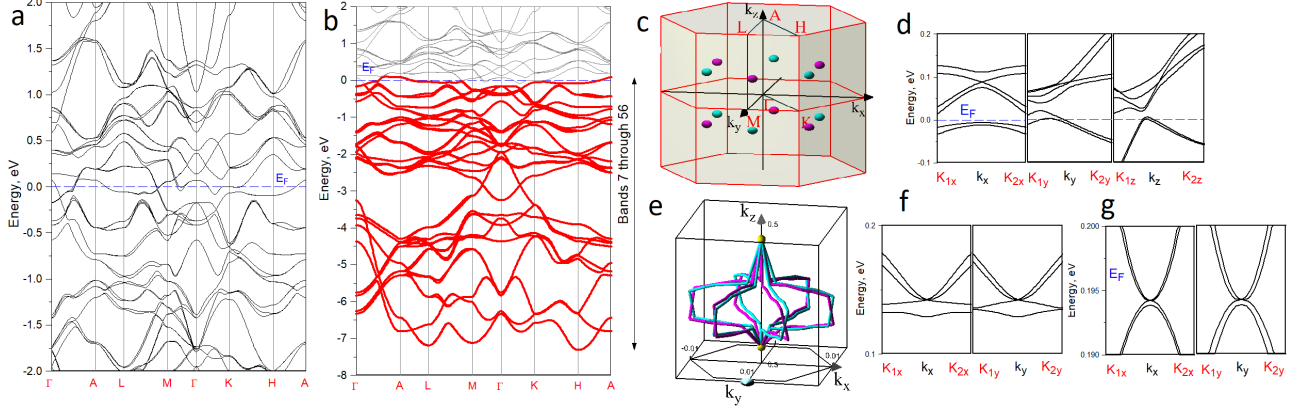


FIG. 7: Results for VAsFe: a. band structure near the Fermi level; b. energy panel used for defining non-Abelian Berry connection; c. positions of low-energy Weyl points; d. energy band dispersions in the vicinity of the Weyl point $k_{wp} = (0.00000, 0.38339, 0.17269)$. Points notations are as follows: $K_{1x} = (-0.10000, 0.38339, 0.17269)$, $K_{2x} = (0.10000, 0.38339, 0.17269)$, $K_{1y} = (0.0000, 0.28339, 0.17269)$, $K_{2y} = (0.0000, 0.48339, 0.17269)$, $K_{1z} = (0.0000, 0.38339, 0.07269)$, $K_{2z} = (0.0000, 0.38339, 0.27269)$ in units $2\pi/a, 2\pi/a, 2\pi/c$; e. nodal lines with triple degenerate points. The zoomed area of the BZ is bounded by $0.3 \leq 2\pi k_z/c \leq 0.5$ and $-0.01 \leq 2\pi k_{x,y}/a \leq +0.01$; f. energy band dispersions in the vicinity of the triple point $k_{ttp} = (0.00000, 0.00000, 0.32279)$. Points notations are as follows: $K_{1x} = (-0.10000, 0.0000, 0.32279)$, $K_{2x} = (0.10000, 0.0000, 0.32279)$, $K_{1y} = (0.0000, -0.1000, 0.32279)$, $K_{2y} = (0.00000, 0.1000, 0.32279)$. in units $2\pi/a, 2\pi/a, 2\pi/c$; g. energy band dispersions in the vicinity of the triple point $k_{ttp} = (0.00000, 0.00000, 0.47625)$. Point notations are as follows: $K_{1x} = (-0.10000, 0.0000, 0.47625)$, $K_{2x} = (0.10000, 0.0000, 0.47625)$, $K_{1y} = (0.0000, -0.1000, 0.47625)$, $K_{2y} = (0.00000, 0.1000, 0.47625)$. in units $2\pi/a, 2\pi/a, 2\pi/c$. Lattice parameters used: $a=11.7352$ a.u., $c/a=0.56892$ [9].

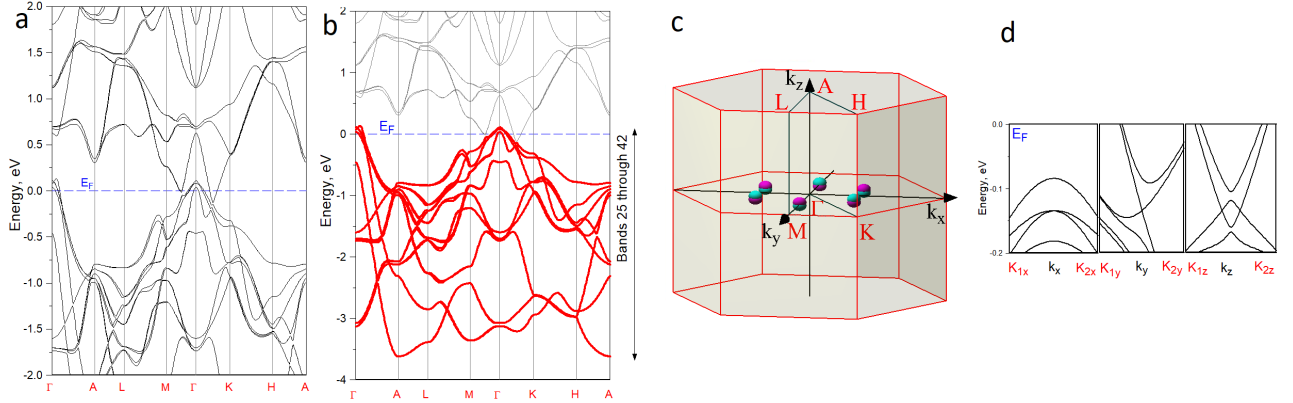


FIG. 8: Results for YGeLi: a. band structure near the Fermi level; b. energy panel used for defining non-Abelian Berry connection; c. positions of low-energy Weyl points as well as d. energy band dispersions in the vicinity of the Weyl point $k_{wp} = (0.00000, 0.27793, 0.00817)$. Point notations are as follows: $K_{1x} = (-0.10000, 0.27793, 0.00817)$, $K_{2x} = (0.10000, 0.27793, 0.00817)$, $K_{1y} = (0.0000, 0.17793, 0.00817)$, $K_{2y} = (0.0000, 0.37793, 0.00817)$, $K_{1z} = (0.0000, 0.27793, -0.04085)$, $K_{2z} = (0.0000, 0.27793, 0.04085)$ in units $2\pi/a, 2\pi/a, 2\pi/c$. Lattice parameters used: $a=13.3509$ a.u., $c/a=0.59915$ [10].

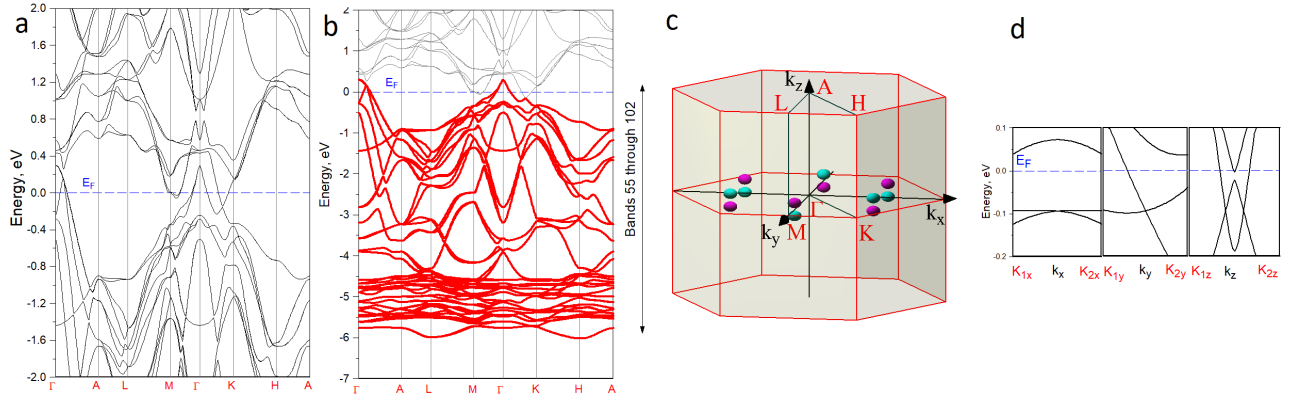


FIG. 9: Results for YPbAg: a. band structure near the Fermi level; b. energy panel used for defining non-Abelian Berry connection; c. positions of low-energy Weyl points as well as d. energy band dispersions in the vicinity of the Weyl point $k_{wp} = (0.00000, 0.40335, 0.03142)$. Point notations are as follows: $K_{1x} = (-0.10000, 0.40335, 0.03142)$, $K_{2x} = (0.10000, 0.40335, 0.03142)$, $K_{1y} = (0.00000, 0.30335, 0.03142)$, $K_{2y} = (0.00000, 0.50335, 0.03142)$, $K_{1z} = (0.00000, 0.40335, -0.15710)$, $K_{2z} = (0.00000, 0.40335, 0.15710)$ in units $2\pi/a, 2\pi/a, 2\pi/c$. Lattice parameters used: $a=14.140$ a.u., $c/a=0.59133$ [11].

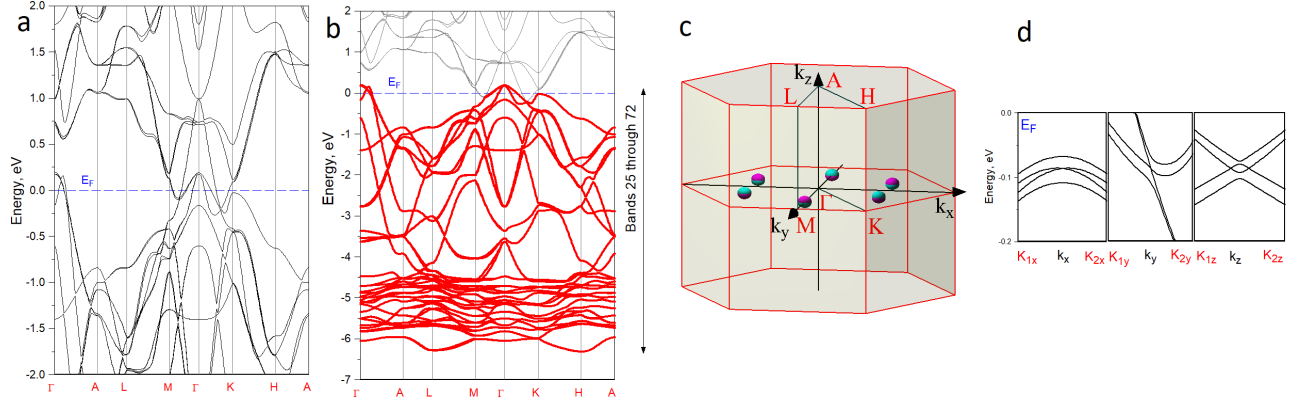


FIG. 10: Results for YSiAg: a. band structure near the Fermi level; b. energy panel used for defining non-Abelian Berry connection; c. positions of low-energy Weyl points as well as d. energy band dispersions in the vicinity of the Weyl point $k_{wp} = (0.00000, 0.37866, 0.00385)$. Point notations are as follows: $K_{1x} = (-0.10000, 0.37864, 0.00385)$, $K_{2x} = (0.10000, 0.37864, 0.00385)$, $K_{1y} = (0.00000, 0.27864, 0.00385)$, $K_{2y} = (0.00000, 0.47864, 0.00385)$, $K_{1z} = (0.00000, 0.37864, -0.0192)$, $K_{2z} = (0.00000, 0.37864, 0.0192)$ in units $2\pi/a, 2\pi/a, 2\pi/c$. Lattice parameters used: $a=13.2623$ a.u., $c/a=0.59364$ [12].

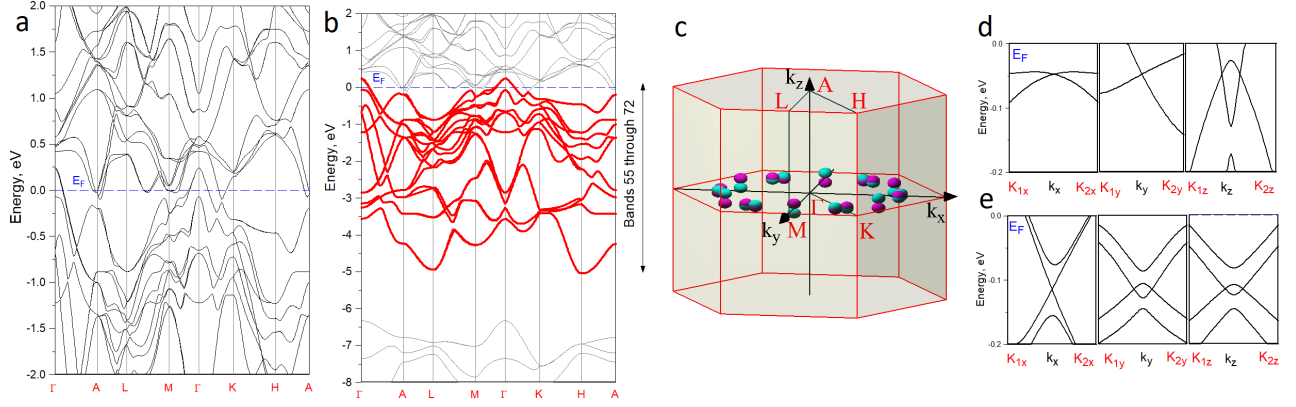


FIG. 11: Results for YTiMg: a. band structure near the Fermi level; b. energy panel used for defining non-Abelian Berry connection; c. positions of low-energy Weyl points; d. energy band dispersions in the vicinity of the Weyl point $k_{wp} = (0.00000, 0.43303, 0.02319)$. Points notations are as follows: $K_{1x} = (-0.10000, 0.43303, 0.02319)$, $K_{2x} = (0.10000, 0.43303, 0.02319)$, $K_{1y} = (0.0000, 0.33303, 0.02319)$, $K_{2y} = (0.0000, 0.53303, 0.02319)$, $K_{1z} = (0.0000, 0.43303, -0.11595)$, $K_{2z} = (0.0000, 0.43303, 0.11595)$ in units $2\pi/a, 2\pi/a, 2\pi/c$. e. energy band dispersions in the vicinity of the Weyl point $k_{wp} = (0.44076, 0.02908, 0.00441)$. Point notations are as follows: $K_{1x} = (0.34076, 0.02908, 0.00441)$, $K_{2x} = (0.54076, 0.02908, 0.00441)$, $K_{1y} = (0.44076, -0.14540, 0.00441)$, $K_{2y} = (0.44076, 0.14540, 0.00441)$, $K_{1z} = (0.44076, 0.02908, -0.02205)$, $K_{2z} = (0.44076, 0.02908, 0.02205)$ in units $2\pi/a, 2\pi/a, 2\pi/c$. Lattice parameters used: $a=14.1824$ a.u., $c/a=0.61272$ [5].

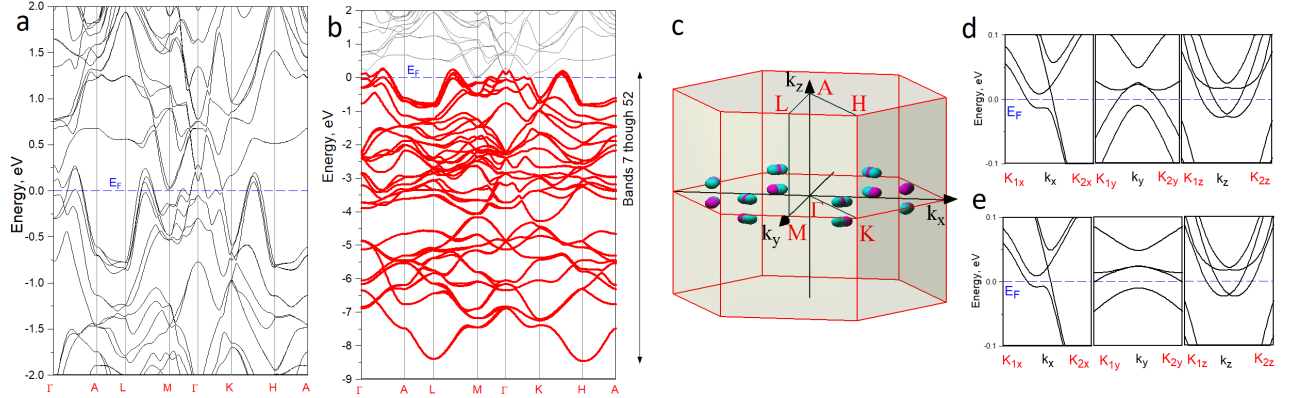


FIG. 12: Results for ZrAsOs: a. band structure near the Fermi level; b. energy panel used for defining non-Abelian Berry connection; c. positions of low-energy Weyl points; d. energy band dispersions in the vicinity of the Weyl point $k_{wp} = (0.47365, 0.02591, 0.04792)$. Points notations are as follows: $K_{1x} = (0.37365, 0.02591, 0.04792)$, $K_{2x} = (0.57365, 0.02591, 0.04792)$, $K_{1y} = (0.47365, -0.12955, 0.04792)$, $K_{2y} = (0.47365, 0.12955, 0.04792)$, $K_{1z} = (0.47365, 0.02591, -0.11980)$, $K_{2z} = (0.47365, 0.02591, 0.11980)$ in units $2\pi/a, 2\pi/a, 2\pi/c$; e. energy band dispersions in the vicinity of the Weyl point $k_{wp} = (0.47406, 0.01215, 0.04789)$. Point notations are as follows: $K_{1x} = (0.37406, -0.01215, 0.04789)$, $K_{2x} = (0.57406, -0.01215, 0.04789)$, $K_{1y} = (0.47406, -0.06075, 0.04789)$, $K_{2y} = (0.47406, 0.06075, 0.04789)$, $K_{1z} = (0.47406, 0.01215, -0.11973)$, $K_{2z} = (0.47406, 0.01215, 0.11973)$ in units $2\pi/a, 2\pi/a, 2\pi/c$. Lattice parameters used: $a=12.476$ a.u., $c/a=0.57467$ [13].

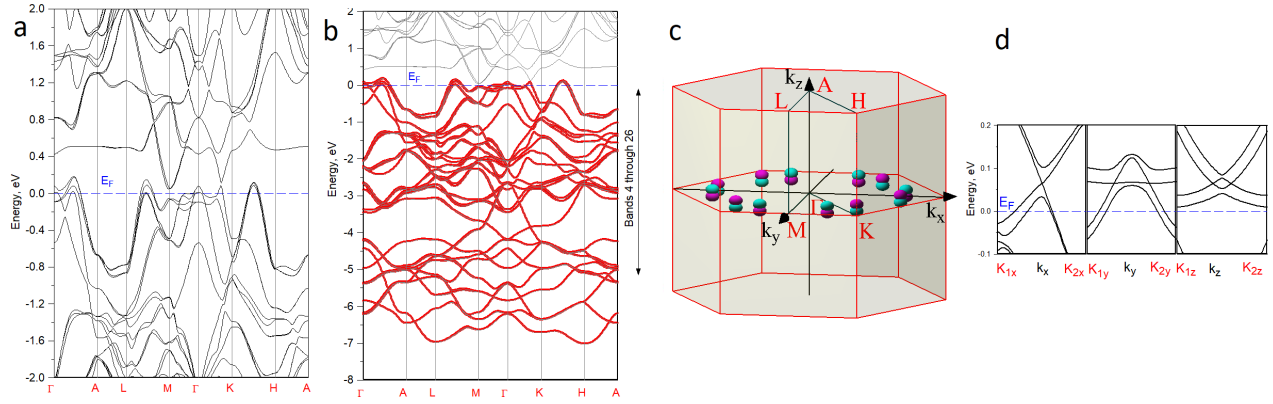


FIG. 13: Results for ZrPRu: a. band structure near the Fermi level; b. energy panel used for defining non-Abelian Berry connection; c. positions of low-energy Weyl points as well as d. energy band dispersions in the vicinity of the Weyl point $k_{wp} = (0.45982, 0.07532, 0.01698)$. Point notations are as follows: $K_{1x} = (0.35982, 0.07532, 0.01698)$, $K_{2x} = (0.55982, 0.07532, 0.01698)$, $K_{1y} = (0.45982, -0.18830, 0.01698)$, $K_{2y} = (0.45982, 0.18830, 0.01698)$, $K_{1z} = (0.45982, 0.07532, -0.0849)$, $K_{2z} = (0.45982, 0.07532, 0.0849)$ in units $2\pi/a, 2\pi/a, 2\pi/c$. Lattice parameters used: $a=12.2057$ a.u., $c/a=0.58492$ [3].

-
- [1] Handbook of Inorganic Substances, edited by Pierre Villars, Karin Cenzual & Roman Gladyshevskii (De Gruyter, 2015).
- [2] G. Kotliar, S. Y. Savrasov, K. Haule, V. S. Oudovenko, O. Parcollet, C.A. Marianetti, Electronic Structure Calculations with Dynamical Mean-Field Theory, *Reviews of Modern Physics* **78**, 865-951, (2006).
- [3] G. P. Meisner, H. C. Ku, The superconductivity and structure of equiatomic ternary transition metal pnictides, *Appl. Phys. A* **31**, 201–212 (1983).
- [4] R. Kraft, M. Valldor, D. Kurowski, R.-D. Hoffmann, and R. Poettgen, Ternary Indides REMgIn (RE = Y, La–Nd, Sm, Gd–Tm, Lu): Synthesis, Structure and Magnetic Properties, *Z. Naturforsch.* 59b, 513–518 (2004).
- [5] R. Kraft and R. Poettgen, Ternary Thallides REMgTl (RE = Y, La – Nd, Sm, Gd – Tm, Lu), *Z. Naturforsch.* 60b, 265–270 (2005).
- [6] D. Johrendt and A. Mewis, Darstellung und Kristallstrukturen der Verbindungen SEPdAs (SE = La-Lu), *J. of Alloys and Comp.* **183**, 210-223 (1992).
- [7] B. Gibson, R. Pöttgen, R. K. Kremer, A. Simon, K. R.A. Ziebeck, Ternary germanides LnAgGe (Ln = Y, Sm, Gd, Lu) with ordered Fe2P-type structure, *J. of Alloys and Comp.* **239**, 34-40 (1996).
- [8] R. Demchyna, Y. Prots and U. Schwarz, Crystal structures of titanium palladium germanium, TiPdGe, two polymorphic modifications, *Z. Kristallogr. NCS* 222 173-174 (2007).
- [9] Mme Roy-Montreuil, B. Deyris et A. Michel, A. Rouault, P. l'Heritier, A. Nylund, J.P. Senateur et R. Fruchart, Nouveaux Composés Ternaires MM'P et MM'As, *Interactions Metalliques et Structures*, *Mat. Res. Bull.* **7**, 813-826, Pergamon Press, Inc. (1972).
- [10] A. Czybulka, G. Steinberg and H.-U. Schuster, Darstellung und Struktur ternärer Silizide und Germanide des Lithiums mit den Seltenen Erden Y und Gd im Fe2P-Typ, *Z. Naturforsch.* 34b, 1057-1058 (1979).
- [11] L.D. Gulay, Crystal structure of RAgPb (R5Y, Er, Tm, Lu) compounds, *J. of Alloys and Comp.* **314** 219–223 (2001).
- [12] I. Savysyuk, O. Shcherban, N. Semuso, R. Gladyshevskii, E. Gladyshevskii, The {Y, Pr}–Ag–Si systems: isothermal sections and crystal structures, *Chem. Met. Alloys* 5 103-112 (2012).
- [13] G. P. Meisner, H. C. Eu, H. Barz, Superconducting Equiatomic Ternary Transition Metal Arsenides, *Mat. Res. Bull.* **18**, 983-991, (Pergamon Press, 1983)